Redox- and EPR-Active Graphene Diiron Complex Nanocomposite

de Sousa, David P.; Yu, Jeffrey Huijie; Miller, Christopher J.; Chang, Yingyue; McKenzie, Christine J.; Waite, T. David

Go to publication entry in University of Southern Denmark's Research Portal

Interfaces: Adsorption, Reactions, Films, Forces, Measurement Techniques, Charge Transfer, Electrochemistry, Electrocatalysis, Energy Production and Storage

A Redox- and EPR-Active Graphene Diiron Complex Nanocomposite

David Poulsen Poulsen de Sousa, Christopher J. Miller, Jeffrey Huijie Yu, Bess Yingyue Chang, Christine J. McKenzie, and T. David Waite

Just Accepted

A Redox- and EPR-Active Graphene Diiron Complex Nanocomposite

David P. de Sousa,[‡#] Jeffrey Huijie Yu,[†#] Christopher J. Miller,[†] Yingyue Chang[†],

Christine J. McKenzie,[‡] and T. David Waite*[,†]

[†] *School of Civil and Environmental Engineering, University of New South Wales, Sydney, NSW 2052, Australia*

[‡] *Department of Physics, Chemistry and Pharmacy, University of Southern Denmark, Campusvej 55, 5230 Odense M (Denmark)*

ABSTRACT: A mixed valence diiron(II/III) complex with the ligand 2,6-bis{bis[(2-pyridinylmethyl)amino]methyl}-phenol (bppH) has been covalently anchored onto graphene using a mild *in situ* microwave-assisted diazonium coupling through an aryl amino precursor and isoamyl nitrite. A dinuclear iron complex is then formed by complexation of the grafted bppH–graphene material with iron(II) in the presence of dioxygen. X-ray photoelectron spectroscopy (XPS), atomic force microscopy, cyclic voltammetry, scanning transmission electron microscopy, energy-dispersive X-ray spectroscopy and electron paramagnetic resonance (EPR) spectroscopy confirms the formation of the anchored ligand and derivative diiron complexes. Semi-quantitative XPS analysis shows an average bppH ligand bulk loading of 0.33 mmol/g, corresponding to a significant 20.7 wt% of the functionalized material consisting of grafted moieties. EPR measurements reveal the existence of a strong isotropic $S = 1/2$ spin center associated with the graphene lattice, together with a much weaker $S = 5/2$ signal, associated with the iron(III) center of the grafted complex. The grafted complex is redox-active with surface-confined $Fe^{II}Fe^{II} \rightarrow Fe^{II}Fe^{III}$ (+0.56 V *vs*. NHE), $Fe^{II}Fe^{III} \rightarrow Fe^{III}Fe^{III}$ (+0.73 V) and $Fe^{III}Fe^{III} \rightarrow Fe^{III}Fe^{IV}$ (+0.95 V) redox processes accessible, with an estimated surface coverage of 58 pmol cm^{-2} established from the electrochemical measurements.

INTRODUCTION

The extraordinary electrical and mechanical properties of single-layered graphene[1] makes it an ideal substrate for surface decoration with redox-active moieties such as transition metal complexes. Redox-active materials based on the surface-decoration of graphene with organic and transition-metal functionalities represents an as yet largely unexplored class of graphene-based nanocomposite materials[2–5], which can be envisaged to be useful in areas as diverse as energy-storage, electrochemically-assisted catalysis and development of micron-sized arrays and sensor devices.[6–9] Such a class of nanocomposite materials would be able to form a bridge between molecular devices and conventional heterogeneous materials - taking the best from both worlds in terms of the activity and selectivity of the molecular designs in combination with the stability, processability and scalability of heterogeneous materials.[5,10]

While some examples exist of covalent functionalization of graphene and other carbon-based materials, such as carbon nanotubes, with small molecules such as the diazonium salts of aniline and its *para*-substituted derivatives,[11–14] to date only a few examples exist showing that it is possible to attach more elaborate, and potentially more interesting and functionally active assemblies.[15–18] These examples include photoelectrochemically active cobalt phthalocyanines covalently anchored onto graphene-type materials,[15,19–21] $RuCl_2(PPh_3)_3$ attached to graphene for use in hydrogenation catalysis,[22] and tris(bipyridine)-ruthenium(II) for photo-induced electrochemical sensing and hydrogenation catalysis.[23,24] Iron coordination complexes tend to show greater lability compared to the aforementioned systems. This is certainly reflected by the fact that the presence of iron in metalloenzymes is extensive. A few relatively stable iron(II)-based systems have all been anchored onto graphene. These include Fe^{II}-terpyridine-complexes,[25,26] ferrocene,[16,27,28] and ferric porphyrin.[29] For iron, these are rigid and stable complexes. No examples with more redox-flexible and less rigid iron-complexes, i.e., non-heme iron type complexes, have been reported to date.

In this work, chemically converted graphene with 13.6 atom% O, resulting from the presence of oxygen-bearing functionalities, was selected for investigation as this bulk graphene derives from non-graphitic precursors processed via a scalable, low-cost and thus more sustainable solvo-thermal method.[30–32] Microwave-assisted exfoliation and diazonium-based coupling strategies are emerging as one the most practical means of covalently modifying carbon-

based materials.[13,33,34] This is due to the relatively mild conditions and the wide range of solvents tolerated (including water). Futher the diazonium salts can be generated *in situ*, which is especially convenient from a synthetic perspective.[12,35]

Scheme 1. Molecular structures of substituted R_1-bppH and derived bis-acetate and bis-(aquo-hydroxo) iron(II)-iron(III) complexes of R_1-bpp⁻

R_1 = NO$_2$, *p*-nitro-bppH
R_1 = NH$_2$, *p*-amino-bppH
R_1 = *tert*-butyl, *tert*-butyl-bppH

4 H$_2$O → 2 HOAc

R_2 = *tert*-butyl, [Fe$_2$(tert-butyl-bpp)(OAc)$_2$]$^{2+}$ and derivative after hydrolysis, [Fe$_2$(tert-butyl)(OH)$_2$(H$_2$O)$_2$]$^{2+}$ ("resting state" in Scheme 3)

R_2 = graphene, [Fe$_2$(graphene–bpp)(OAc)$_2$]$^{2+}$ and derivative after hydrolysis, [Fe$_2$(graphene–bpp)(OH)$_2$(H$_2$O)$_2$]$^{2+}$ ("resting state" in Scheme 3)
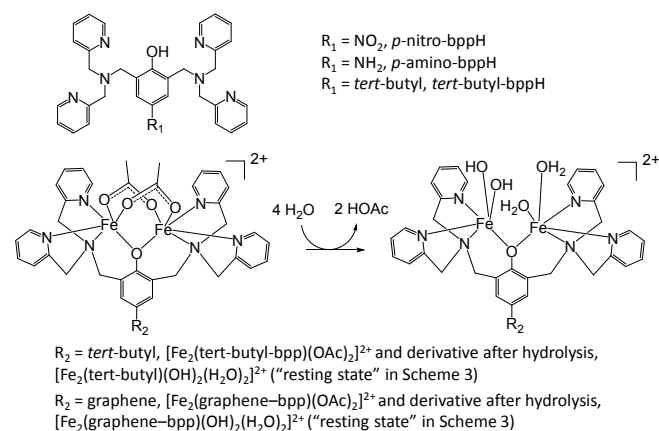
The phenolate-hinged dinucleating 2,6-bis{[bis(2-pyridylmethyl)amino]methyl}-phenolato(1-)Fe^{III}Fe^{II} complex core (Fe$_2$(bpp)), Scheme 1, was selected for use in this study. A range of transition metal complexes based on this scaffold, such as 2,6-bis{[bis(2-pyridylmethyl)amino]methyl}-4-(*tert*-butyl)-phenolato(1-) (abbreviated in this work as *tert*-butyl-bpp, Scheme 1) with Fe[36–38] and Mn[39] have previously been reported as models for both the structure and redox reactivity of metalloenzymes (such as purple acid phosphatase and catalase). Additionally, the crystal- and molecular structures of various binuclear iron and 4-(*tert*-butyl)-bpp complexes are known and the molecular properties have been studied in detail.[36–38]

The elemental composition, the degree of grafting and the nature of the covalent linkers, together with the electrochemical properties of the grafted complex, have been examined in detail using a battery of techniques including X-ray photoelectron spectroscopy (XPS), atomic force microscopy (AFM), cyclic voltammetry (CV), scanning transmission electron microscopy (STEM), energy-dispersive X-ray spectroscopy (EDX), Time of Flight Secondary Ion Mass Spectrometry (ToF-SIMS) and electron paramagnetic resonance (EPR).

EXPERIMENTAL SECTION

Materials. Unless otherwise noted, commercially available reagents were purchased from Sigma-Aldrich or Alfa Aesar and used without further purification. All organic solvents were of spectrophotometric or HPLC Plus grade and used without further purification. All other reagents employed in this study were of analytical grade. Bis(2-pyridylmethyl)amine and [Fe^{II}Fe^{III}(*tert*-butyl-bpp)(CH$_3$CO$_2$)$_2$](ClO$_4$)$_2$ (*tert*-butyl-bpp = 2,6-bis{[bis(pyridin-2-ylmethyl)amino]methyl}-4-(*tert*-

butyl)phenolate) were prepared according to literature procedures.[36,38] Aqueous solutions were prepared using 18 MΩ cm water from a Millipore Milli-*Q* system. Electrolyte solutions were prepared using 99.99% NaClO$_4$·H$_2$O. Carbon adhesives and copper grids (400-mesh) for electron microscopy, silicon wafers for ToF-SIMS, mica for AFM and indium foil for XPS were purchased from Ted Pella. Graphene powder (83 *wt*% carbon) was purchased from Carbon Allotropes (Australia) and used as received.

Instrumentation. Elemental analyses were performed at the Chemistry Department at Copenhagen University. IR spectra were recorded on a PerkinElmer Spectrum Two ATR FT-IR spectrometer. ^{1}H- and ^{13}C-NMR spectra were recorded on a Bruker AVANCE III 400 spectrometer. Microwave reactions were performed in an Anton Paar Monowave 300 Microwave Reactor under argon. Electrospray Ionization (ESI) mass spectra were recorded on a nanospray MS Bruker micrOTOF-Q II spectrometer. EPR spectra were recorded on a Bruker EMX Plus X–band CW spectrometer using an ER 4103 TM110 cavity. CVs were recorded on a CH Instruments 600D electrochemical analyzer using a standard 3-electrode setup with a glassy carbon disk (nominal diameter: 0.3 cm) working electrode, a Pt wire counter electrode and an Ag/AgCl (3 M KCl) reference electrode. The working electrode was polished with alumina (0.05 μm) and sonicated in methanol and water prior to use. Potentials were referenced to the NHE by adding +0.25 V. This calibration value was determined using the [Fe^{III}(CN)$_6$]$^{3-}$/[Fe^{II}(CN)$_6$]$^{4-}$ couple (10 mM, 0.5 M KCl, $E_{1/2}$ = 0.456 V *vs*. NHE)[40] as standard. The electrochemically active surface area of the working electrode was estimated at 0.12 cm² using K$_3$[Fe^{III}(CN)$_6$] as a probe. Hexacyanoferrate can show sensitivity to the surface chemistry of the working electrode as its main mechanism of action during electron transfer is outer-sphere in nature.[41] This can result in the electrochemically active surface area being underestimated. Aqueous working conditions are employed in this study, thus more inert electron-transfer probes such as ferrocene, [Ru(NH$_3$)$_6$]$^{3+}$ or [Os(bpy)$_3$]$^{2+}$ (bpy = 2,2′-Bipyridine) could not be utilized, due to the lack of hydration stability and solubility, respectively, in aqueous solution. All peak currents and peak potentials were obtained through Gaussian curve deconvolution with corresponding polynomial or spline background subtraction.

XPS spectra were recorded on a Thermo ESCALAB250Xi instrument with samples manually pressed onto In foil and irradiated under vacuum with monochromatic Al Kα radiation (1486.68 eV). Spectra were deconvoluted using a Shirley background correction and peaks fitted using pseudo-Voight line shapes. STEM/EDX analyses were performed on either a Philips CM200 instrument (operated at 200 keV) equipped with a field emission gun (extraction voltage set at 4.48 kV) interfaced with a Bruker QUANTAX EDX spectrometer or on a FEI Tecnai G² 20 instrument (operated at 200 keV) interfaced with an XFlash 6|30 EDX detector and a MOXTEK AP3.3 super light element window. AFM measurements were made on a Bruker

2

Dimension Icon SPM instrument operated in PeakForce tapping mode with a Bruker SCANASYST-AIR probe. Time of Flight Secondary Ion Mass Spectrometer (ToF-SIMS) analyses were carried out with an ION-TOF TOF.SIMS 5 spectrometer. Surface analysis was performed in static positive secondary ion mode. Spectra were acquired using Bi^+ as the primary ion projectile at a dose of ~6.37×10^8 ions/cm^2 at 30 keV which was rastered on a 100×100 µm^2 surface area. All SIMS spectra were calibrated internally to signals of $[C_4H_9]^+$, $[C_3H_7]^+$, $[C_2H_5]^+$, or $[CH_3]^+$.

Theoretical surface coverage calculations. The theoretical maximally obtainable surface coverage of the bppH ligand on graphene was calculated using the model compound *tert*-butyl-bppH to estimate the distance (H) of sp^3-C from graphene to the far end of the bppH ligand and to calculate the radius (*r*) of the bppH ligand. The geometry of Fe$_2$(bpp) grafted on graphene was estimated using the analogous molecular structure of acetate-bridged [Fe^{II}Fe^{III}(*tert*-butyl-bpp)(CH$_3$CO$_2$)$_2$](ClO$_4$)$_2$ derived from single-crystal X-ray diffraction.[36]

The theoretical maximally attainable surface coverage value (Γ, expressed in mol cm^{-2}) for a bppH monolayer on graphene was estimated assuming that bppH ligands form a hexagonal close packed monolayer on one of the graphene surfaces (Equation 1):[42]

$$\Gamma = \frac{1.92 \times 10^{-8}}{(2r)^2}$$

<div align="right">Equation 1</div>

Here *r* (in Å) is the radius of the cylinder, which represents the volumetric container confining a steric bppH group with a rotation of the widest pyridyl moieties along the central phenoxy axis. Such a model is valid for materials where the functionalization process is governed by steric repulsion effects and where the host material does not predominantly exist as single sheets but are stacked in layers, leaving, on average, only one side of the sheets free to be functionalized. This enables a calculation of the theoretical maximally attainable surface coverage for bppH on graphene of 82 pmol cm^{-2}.

Sodium   4-nitro-2,6-bis[(bis(2-pyridylmethyl) amino)]-methylphenolate (Na[*p*-nitro-bpp]). Bis(2-pyridylmethyl) amine (16.4 g, 82.3 mmol), 4-nitrophenol (2.89 g, 20.8 mmol) and *para*-formaldehyde (2.71 g, 90.2 mmol) were dispersed in 50 % *aq*. ethanol and refluxed for 9 days under dry nitrogen. The resulting reddish-brown solution was reduced in volume by rotary evaporation and the pH of the residual aqueous suspension adjusted to ~10 with NaOH pellets. The alkaline suspension was extracted with ethyl acetate (4×120 mL) and the combined organic phases dried (Na$_2$SO$_4$), gravity filtered and rotary evaporated to leave a light brown oil. The oil was triturated with diethyl ether (4×80 mL) to give a mustard coloured solid. Recrystallization from boiling acetone gave a canary yellow solid (8.85 g, 72 %). R_f (SiO$_2$, acetone) = 0.32. Anal. Calc. for C$_{32}$H$_{30}$N$_7$NaO$_3$: C, 65.86; H, 5.18; N, 16.80. Found: C, 65.16; H, 5.30; N, 15.95. ^{1}H NMR (400 MHz, DMSO-d_6), δ

(ppm): 8.47 (d, J = 4.1 Hz, 4H, PyH), 8.03 (s, 2H, ArH), 7.74 (td, J = 7.7, 1.6 Hz, 4H, PyH), 7.56 (d, J = 7.8 Hz, 4H, PyH), 7.23 – 7.19 (m, 4H, PyH), 3.71 (s, 8H, 4CH$_2$), 3.46 (s, 4H, 2CH$_2$). ^{13}C NMR (100 MHz, DMSO-d_6), δ (ppm): 178.3, 159.5, 148.7, 136.5, 127.5, 125.9, 125.3, 122.3, 121.8, 59.8, 53.9. ESI-MS(CH$_3$CN), m/z: 363.15 ([(M^- – NH(CH$_2$Py)$_2$) + 2H]$^+$, 79%), 562.25 ([M^- + 2H]$^+$, 100%), 584.25 ([M^- + Na + H]$^+$, 29%). Spectra available in Supplementary Information (Figures S1, S2 and S3).

4-amino-2,6-bis[(bis(2-pyridylmethyl)amino)] methyl-phenol (*p*-amino-bppH). Sodium 2,6-bis[(bis(2-pyridylmethyl)amino)methyl]-4-nitrophenolate (5.00 g, 8.9 mmol) was dispersed in absolute ethanol (200 mL). The reaction flask was evacuated, followed by flushing with dry nitrogen. A slurry of 10% Pd/C (428 mg) in dichloromethane (10 mL) was added and the system evacuated and flushed with H$_2$. The suspension was stirred at ambient temperature for 19 h. Celite (3 g) and water (2 mL) were added and the slurry filtered off by vacuum filtration on a Buchner funnel. The filter cake was washed clean with acetone and the combined filtrates further subjected to gravity filtration to give a clear yellow solution. Rotary evaporation of the solution followed by drying under vacuum afforded the product as a dark brown viscous oil (4.59 g, 97%). ^{1}H NMR (400 MHz, DMSO-d_6), δ (ppm): 8.50 (d, J = 4.8 Hz, 4H, PyH), 7.73 (td, J = 7.7, 1.8 Hz, 4H, PyH), 7.49 (d, J = 7.8 Hz, 4H, PyH), 7.26 – 7.23 (m, 4H, PyH), 6.54 (s, 2H, ArH), 3.75 (s, 8H, 4CH$_2$), 3.59 (s, 4H, 2CH$_2$). ^{13}C NMR (100 MHz, DMSO-d_6), δ (ppm): 158.3, 148.3, 146.1, 139.5, 136.1, 123.6, 122.2, 121.7, 114.8, 58.5, 53.6. ESI-MS (CH$_3$CN), m/z: 200.12 ([NH(CH$_2$Py)$_2$ + H]$^+$, 32%), 333.17 ([(M – NH(CH$_2$Py)$_2$) + H]$^+$, 100%), 355.15 ([(M – NH(CH$_2$Py)$_2$) + Na]$^+$, 21%), 373.20 (99%), 532.26 ([M + H]$^+$, 54%), 554.26 ([M + Na]$^+$, 19%), 572.31 (44%), 594.29 (12%). IR (NaCl film), v (cm^{-1}): 1717 (w), 1596 (s, br), 1567 (s), 1472 (vs, br), 1430 (vs, br), 1364 (s), 1261 (m), 1122 (m), 1217 (m), 1000 (w), 767 (w). Spectra available in Supplementary Information Figure S4, S5 and S6.

{2,6-bis[(bis(2-pyridinylmethyl)amino)methyl]-phenol}-graphene (graphene–bppH). Graphene (10 mg, 0.83 mmol) and sodium dodecyl sulfate (1 mL from a 1 mg/mL stock, 4 µmol) was dispersed in 3:2 acetonitrile/water (37 mL) by sonication for 30 min. After purging the solution with argon, *p*-amino–bppH (222 mg, 0.42 mmol) and isoamyl nitrite (84 µL, 0.63 mmol) were added and the suspension stirred for a further 2 h in the dark under an atmosphere of argon. The reaction mixture was transferred under an atmosphere of argon to a microwave vial and microwave irradiated under stirring (200 W, 60 °C) for 160 min. After cooling to ambient temperature, the crude graphene powder was isolated by vacuum filtration (PTFE membrane, 0.2 µm) and washed extensively with dimethylformamide, ethanol, acetonitrile, methanol, and finally acetone through dozens of cleaning cycles with dispersion, sonication and filtration (3×20 mL per solvent). Drying under vacuum (75 °C, 8 h) afforded the product as a black solid (9 mg).

Physisorbed *p*-amino-bppH/graphene. Prepared using the same protocol as for graphene–bppH, with the exception that no isoamyl nitrite was added.

[Fe₂(graphene–bpp)(CH₃CO₂)₂]²⁺

(Fe₂(graphene–bpp)). graphene–bppH (7.6 mg) was dispersed in methanol (7.6 mL) by sonication for 15 min. Fe(ClO₄)₂(H₂O)$_x$ (150 µL from a ~40 mM stock, ~6 µmol) and sodium acetate (400 µL from a 50 mM stock, 20 µmol) was added. After stirring overnight in air, the product was isolated by vacuum filtration (PTFE membrane, 0.2 µm), washed thoroughly with methanol and dried under vacuum (100 °C) to afford the product as a black solid (7 mg).

Physisorbed FeOx/graphene. Prepared using the same protocol as for loading graphene–bppH with Fe, except for the use of unfunctionalized graphene.

Samples for surface analyses. Graphene and functionalized graphene samples were suspended in methanol (~0.1 mg/mL) by gentle sonication and drop-cast onto appropriate solid supports followed by drying in air under an infrared lamp. Silicon wafers were used for ToF-SIMS. Copper grids coated with holey or lacey carbon adhesive were used as supports for STEM. Freshly cleaved mica was used as the substrate for AFM.

Optimization of grafting conditions with *N*-(4-amino-2-chlorophenyl)acetamide. Graphene (10 mg, 0.83 mmol) was dispersed in the exfoliation medium (26 mL, see Table 1) by sonication for 30 min. After purging the solution with argon, *N*-(4-Amino-2-chlorophenyl)acetamide (77 -154 mg, 0.42 - 0.84 mmol, see See Table 1) and isoamyl nitrite (84 - 169 µL, 1.25 - 0.63 mmol) were added and the suspension stirred for a further 2 h in the
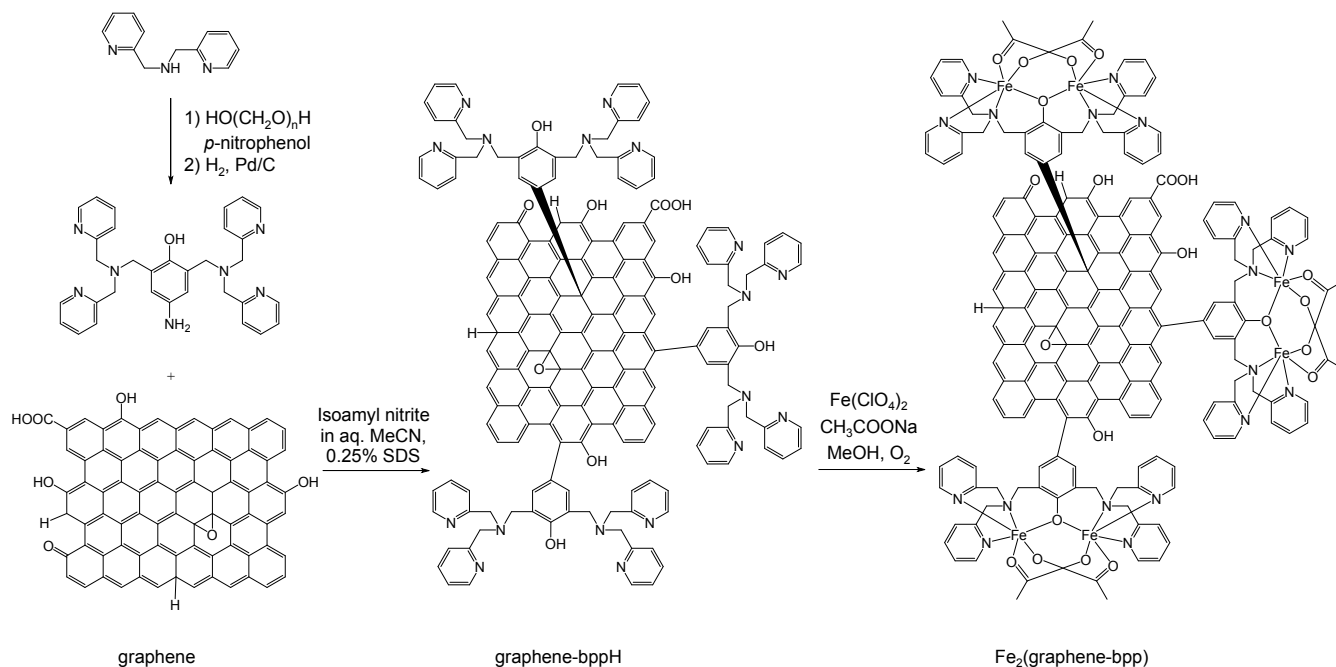
dark under an atmosphere of argon. Depending on the reaction conditions (See Table 1), the reaction mixture was either heated in an oil-bath under an atmosphere of argon under stirring at 65 °C for 25 h or transferred under an atmosphere of argon to a microwave vial and microwave irradiated under stirring (100 W, 60 °C) for 90 min. After cooling to ambient temperature, the crude graphene powder was isolated by vacuum filtration (PTFE membrane, 0.2 µm) and washed extensively with dimethylformamide, ethanol, acetonitrile, methanol, and finally acetone through dozens of cleaning cycles with dispersion, sonication and filtration (3×20 mL per solvent) and dried under vacuum.

Table 1. Pilot experiments with *N*-(4-amino-2-chlorophenyl)acetamide for optimizing grafting conditions.

#	Solvent	Conditions	C : Aniline: Nitrite [2]	SDS
1	3:2 CH₃CN/H₂O	Thermal	4:2:3	Yes
2	2:3 CH₃CN/ODBC	Thermal	4:2:3	No
3	3:2 CH₃CN/H₂O	Thermal	2:2:3	Yes
4	2:3 CH₃CN/ODBC	Thermal	2:2:3	No
5	3:2 CH₃CN/H₂O	Microwave	4:2:3	Yes
6	2:3 CH₃CN/ODBC	Microwave	4:2:3	No

[1] ODBC: 1,2-dichlorobenzene. [2] C: Aniline: Nitrite, represents the molar ratio of carbon from graphene (assuming all 10 mg of graphene used consisting of pure carbon), *N*-(4-Amino-2-chlorophenyl)acetamide, and isoamyl nitrite.

Scheme 2. Synthesis and coupling of p-amino-bppH on graphene and complexation of grafted bppH with iron(II)/iron(III).

1) HO(CH₂O)ₙH
p-nitrophenol

2) H₂, Pd/C

NH₂

+

graphene

HOOC

OH

HO

H

O

H

Isoamyl nitrite
in aq. MeCN,
0.25% SDS

OH

OH

COOH

OH

H

O

OH

graphene-bppH

Fe(ClO₄)₂
CH₃COONa
MeOH, O₂

OH

OH

COOH

OH

O

OH

Fe₂(graphene-bpp)

Modified carbon electrodes. Fe₂(graphene–bpp) (3 mg) and Nafion-117 (43 µL of a 5 wt% stock, ~6.5 mg) in methanol (157 µL) were sonicated for 15 min until a homogeneous ink was formed. The ink (~5 µL) was drop-cast onto a freshly cleaned glassy carbon surface (3 mm) and allowed to dry in air. The modified electrodes were activated by several successive scans at 200 mV s⁻¹ in 0.1 M *aq*. NaClO₄ until the voltammograms stabilized. Controls of glassy carbon/nafion electrodes with unfunctionalized graphene and FeOx/graphene were prepared similarly.

RESULTS AND DISCUSSION

Initial Optimization of Grafting Conditions

The optimal conditions for the diazonium grafting, were determined initially, using *N*-(4-amino-2-chlorophenyl) acetamide as a elemental probe, by systematically varying the reaction medium, the reagent stochiometry and the heating source. Commercially available *N*-(4-amino-2-chlorophenyl) acetamide was used as probe due to its *N*- and Cl-content. The corresponding diazonium salt was generated *in situ* using isoamyl nitrite, which is soluble in organic solvents. The effectiveness of the different grafting conditions were evaluated using XPS spectroscopy in order to determine the N and Cl content of the grafted graphene materials under these different conditions (See Table 1 and Supplementary Information Table S1 and Figure S7). These pilot studies revealed that a combination of aqueous acetonitrile with surfacant as the medium and microwave-assisted heating provided the best conditions for efficient functionalization of graphene.

Preparation of graphene–bppH and Fe₂(graphene–bpp)

The covalent attachment of bppH onto graphene was achieved using the optimized microwave-assisted diazonium coupling conditions, determined above.

Scheme 2 outlines the grafting protocol, where the diazonium salt is generated *in situ* from isoamyl nitrite and the *p*-amino phenol derivative of bppH (*p*-amino-bppH). Whilst *p*-amino-bppH is a known compound,[43] the previously reported synthesis proved unfeasible for gram scale preparations so a new scalable synthesis was devised. Briefly, we first prepared the sodium salt of the *p*-nitro phenol derivative in good yields through a one-pot Mannich reaction. The nitro group was then reduced with hydrogen over Pd/C to give *p*-amino-bppH in almost quantitative yield.

Complexation of graphene–bppH with iron(II) and iron(III) was carried out under non-aqueous conditions using iron(II)-diperchlorate in the presence of O₂ and sodium acetate, yielding Fe₂(graphene–bpp).

Surface characterization of Fe₂(graphene–bpp)

STEM-EDX measurements of the exfoliated Fe₂(graphene–bpp) revealed that the material consists of two different populations of graphene sheets present in roughly equal amounts, with flakes being either heavily grafted with Fe₂(bpp) moieties, or only very weakly grafted, Figure 1 (and Supplementary Information Figures S8 and S9). This indicates that the graphene sheets were not completely exfoliated during the microwave-assisted functionalization process and, as a consequence, only the surface exposed sheets were optimally functionalized. AFM thickness measurements (ESI, Figure S10) corroborate this and indicate that the unfunctionalized graphene starting material exists in the form of several stacked layers. While AFM is not well-suited for the exact quantification of the numbers of layers, it still provides

5

good qualitative indications.[44] TEM micrographs show that the surface of the Fe_2(graphene–bpp) flakes, which are ~3 μm in diameter, have undergone drastic morphological changes compared to the unfunctionalized and weakly functionalized graphene sheets. Whereas the unfunctionalized graphene flakes exhibit smooth untextured surfaces (ESI, Figure S8), the surfaces of the Fe_2(graphene–bpp) flakes are very rugged and highly wrinkled. On the nanometer scale, these are clearly visible as patterns of very regularly spaced small motifs. The patterning is distinct from that typically observed for deposited nanoparticles, which tend to aggregate into domains (*e.g.* crystalline or amorphous iron oxides, FeOx).[45–47] Selected area electron diffraction (SAED) measurements reveal that the functionalized sheets are amorphous or weakly polycrystalline, consistent with partial disruption of the π-conjugated matrix due to the heavy functionalization. Energy-dispersive X-ray (EDX) spectroscopy (Figure 2) confirms the findings from STEM. Interestingly, the EDX maps clearly show that the *N* and Fe content, while distributed through all of the Fe_2(graphene–bpp) flakes, are most intensely associated with the wrinkles and edges of the flakes. This suggests that edge functionalization is the most predominant functionalization mode, with the inner parts only functionalized to a lesser degree. This is likely due to steric effects.[48]

ToF-SIMS measurements (ESI, Figures S11) on Fe_2(graphene–bpp) reveal several pyridyl-related fragment ions, associated with the bppH ligand (assignments in ESI, Figure S12 and Tables S2-4), at *m/z* = 91.06 ($[C_6H_5N]^+$, relative abundance = 9.5 %), 92.06 ($[C_6H_6N]^+$, 79.6 %), 93.06 ($[C_6H_7N]^+$, 65.3 %), 133.06 ($[C_8H_9N_2]^+$, 11.9 %), 147.09 ($[C_9H_{11}N_2]^+$, 20.9 %) and 222.12 ($\{Na[C_{12}H_{13}N_3]\}^+$, 2.2 %) together with relatively weak phenoxy fragment ions at *m/z* = 117.02 ($[C_8H_5O]^+$, 2.1 %) and 119.07 ($[C_8H_7O]^+$, 1.0 %). None of these ions were present in the ToF-SIMS spectra of unfunctionalized graphene.
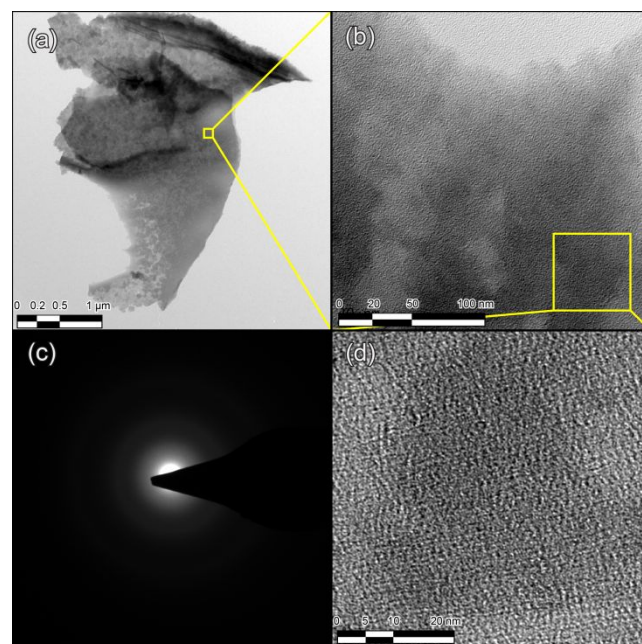
Figure 1. (**a**) TEM image of a selected heavily grafted Fe_2(graphene–bpp) flake. (**b**, **d**) HR TEM images revealing finely patterned surface texture from Fe_2(bpp) grafting. (**c**) Selected area electron diffraction (SAED) pattern, showing absence of diffraction lines. TEM images of unfunctionalized graphene and weakly grafted Fe_2(graphene–bpp) are available in the Supplementary Information (Figure S8 and S9).
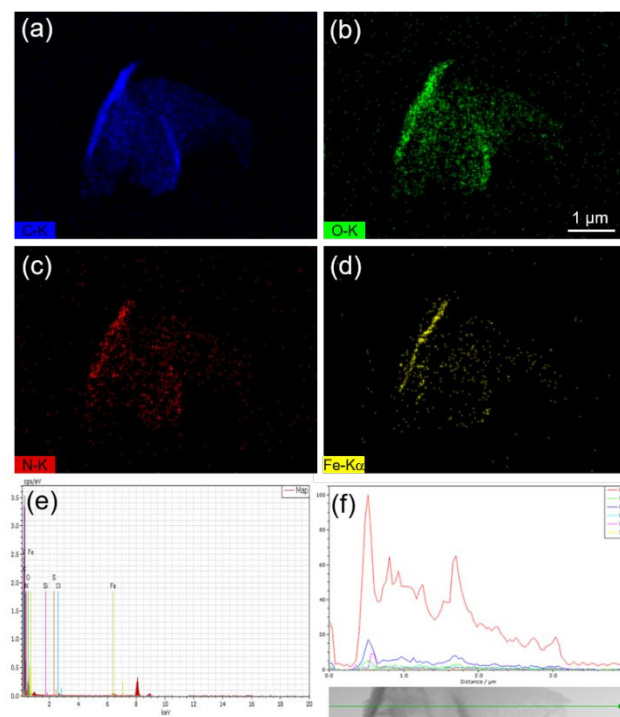
Figure 2. EDX elemental mapping of a selected heavily grafted Fe_2(graphene–bpp) sheet, showing (**a**) Carbon K-edge (blue color), (**b**) Oxygen (green), (**c**) Nitrogen (red), (**d**) Iron (yellow), and corresponding (**e**) energy- and (**f**) line-scan spectra.

An intense signal at $m/z = 55.94$, with an isotope pattern consistent with Fe^+, was also evident in the Fe_2(graphene–bpp) spectra and the molecular reference [Fe_2(*tert*-butyl-bpp)(CH_3CO_2)$_2$](ClO_4)$_2$. Observation of this "naked" Fe^+ ion, indicates that the ionization has been harsh enough to demetallate the complexes.

In the spectra of Fe_2(graphene–bpp), higher molecular weight bppH derived fragment ions and clusters are also evident, at $m/z = 252.01$ ([$C_{14}H_{25}N_3O]^+$, 1.3 %), 267.03 ([$C_{16}H_{17}N_3O]^+$, 1.2 %), 281.01 ([$C_{16}H_{17}N_4O]\}^+$, 5.4 %), 325.07 ([$C_{19}H_{25}N_5O]^+$, 2.0 %), 385.04 ([$C_{23}H_{23}N_5O]^+$, 1.0), 400.01 ([$C_{24}H_{26}N_5O]^+$, 0.70%) and 460.05 ({$Na[C_{27}H_{27}N_5O]\}^+$, 0.36%). An ion at $m/z = 513.07$, consistent with a •bppH fragment ([$C_{32}H_{29}N_6O]^+$) was observed only in the spectra of [Fe_2(*tert*-butyl-bpp)(CH_3CO_2)$_2$]$^{2+}$. This ion was not observed in Fe_2(graphene–bpp). This suggests that the Fe_2(bpp) moieties are strongly anchored to the graphene matrix making simple detachment without partial destruction of the ligand framework impossible.

EPR analysis

The magnetic properties of Fe_2(graphene–bpp) was probed with electron paramagnetic resonance spectroscopy (EPR) (see Figure 3) which revealed the presence of a strong axial low-spin signal at $g' = 1.99$ together with a much weaker high-spin signal at $g' = 4.14$.

EPR activity has often been observed in reduced graphene oxide and functionalized graphene-derived materials and is ascribed either to the presence of stable "edge" states with unpaired electrons, caused by defects,[49,50] or from edge effects due to nanoscale dimensions.[51,52] Given the presence of considerable defects in the π-conjugated graphene lattice due to the functionalization of Fe_2(graphene–bpp) together with the medium-to-broad linewidth of ~5 mT (peak-to-trough), indicative of relatively fast spin-lattice relaxation, and the fact that the low-spin signal is observable even at room temperature, we assign this strong $S = 1/2$ signal to the graphene matrix of Fe_2(graphene–bpp).[49]

The high-spin $g' = 4.14$ signal coincides with that observed for the molecular complex [Fe_2(*tert*-butyl-bpp)(CH_3CO_2)$_2$]$^{2+}$, which gives rise to a rhombic $S = 5/2$ signal due to the iron(III) center in the same magnetic field region. This is consistent with this weak $g' = 4.14$ signal arising from the $S = 5/2$ iron(III) center of the grafted complex. Double integration gives a rough estimate of the iron content, as contributing to <5 % of the total EPR-active content of the sample.

Octahedral Fe(II) centres are silent in X-band EPR spectroscopy, since both the low-spin ($S = 1$) and the high-spin ($S = 2$) configurations will give rise to non-Kramer's doublet ground states. Observation of a high-spin iron(III) signal, indicates either a weakly, or magnetically uncoupled, mixed valence $Fe^{II}Fe^{III}$ ground state or a $Fe^{III}Fe^{III}$ ground state. Formation of a mixed valence core would be consistent with what has previously been observed in the preparation of molecular complexes with *tert*-butyl-bppH. In the presence of air this ligand reacts

with iron(II) and sources of auxiliary ligands (X) to form mixed valence [$Fe^{II}Fe^{III}$(*tert*-butyl-bpp)(X)$_2$]$^{2+}$ complexes.[36,37] The iron centres in the molecular complex, [$Fe^{II}Fe^{III}$(*tert*-butyl-bpp)(CH_3CO_2)$_2$]$^{2+}$ are antiferromagnetically coupled and the coupling constant was measured to be only $J = -4$ cm^{-1}.[36] This explains the non-quenched EPR activity.
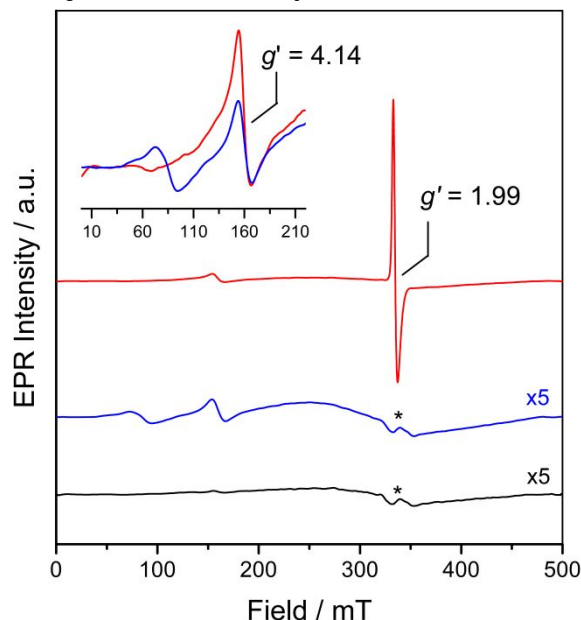

Figure 3. X-band EPR spectra (100 K). Solid-state spectrum of Fe_2(graphene–bpp) (0.5 mg powder, red line), reference spectra: Dissolved [Fe_2(*tert*-butyl-bpp)(CH_3CO_2)$_2$](ClO_4)$_2$ (10 mM in CH_3CN, blue line) and blank spectrum of CH_3CN present (black line). The weak signal marked with asterisk (*) ~340 mT is due to the coil of the thermal probe.

Thus, in analogy to the synthesis of the molecular parent complexes, oxidation of one of the iron(II) centers is proposed to occur through the *in situ* reaction with aerial O_2, Equation 2 ($X^- = CH_3CO_2^-$). Charge neutrality dictates that the divalent complex cation is accompanied by two anions. These can be either perchlorate anions, or they may arise from deprotonation of oxygen functionalities on the graphene (*e.g.* phenolate anions or carboxylate anions).

graphene–bppH + 2 Fe^{2+} + 2 X^- + 1/4 O_2 $\longrightarrow$ [$Fe^{II}Fe^{III}$(graphene–bpp)(X)$_2$]$^{2+}$ + 1/2 H_2O
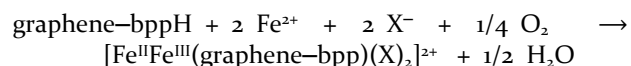
Equation 2

XPS analysis and bulk loading of Fe_2(graphene–bpp)

Quantitative analysis of the XPS spectra was used to estimate the extent of grafting and the types of bonds formed between graphene and the bppH moieties. A summary of the XPS data for graphene–bppH and Fe_2(graphene–bpp) is available in Supplementary Information Figure S13 and Tables S5 and S6. Typical deconvoluted XPS spectra for Fe_2(graphene–bpp) are shown in Figure 4. The XPS data shows that the *N* content

7

of the functionalized samples has increased significantly, compared to the very low *N* content found in unfunctionalized graphene. In graphene–bppH, a strong nitrogen XPS absorption at 400.3 eV is observed together with a minor shoulder at 402.5 eV, which we assign to the pyridyl *N*–sp²C and amine *N*–sp³C bonds, respectively.[53–58] Together they account for 3.2 atm% of the sample. A reference sample with graphene microwave-heated with *p*-amino-bppH in the absence of isoamyl nitrite, showed an *N* content of only 1.7 atm%.

In Fe₂(graphene–bpp), three distinct nitrogen peaks are observed. The dominant *N*-sp²C peak occurs at 400 eV and, accounting for 1.7 atm %, can be associated with the four pyridine donors. Minor shoulders at 399 eV and 402 eV, accounting for 0.4 atm% and 0.3 atm%, respectively are assigned to the two tertiary amines donor groups of bpp. A rationale for the difference observed in their binding energies[39] is due to them bonding to the iron(III) and iron(II) atoms respectively. In Fe₂(graphene–bpp), peaks are also present for both Cl $2p_{3/2}$ at 200.8 eV (0.5 atm%) and Fe $2p_{1/2}/2p_{3/2}$ (711.8-722.5 eV). The Cl content is lower than expected, which could indicate that perchlorate is not the only anion in the sample - possibly a result of the oxygen functionalities in graphene acting as counter-ions (*vide supra*).

The Fe XPS $2p_{1/2}$ and $2p_{3/2}$ region at binding energies from 717.1 to 722.5 eV (Figure 4(d)), exhibits a multitude of peaks including several multiplet splittings[59] and shake-up satellite structures.[60] The richness in the Fe XPS region is as expected for a material containing both high spin Fe^{II} and high-spin Fe^{III} centers, together with the effect from having Fe^{III} and Fe^{II} centers coordinated to both pyridyl, amine and acetate ligands. The extensive overlapping of the Fe $2p_{3/2}$ photoelectron peaks renders delineation and differentiation between the Fe^{III} and Fe^{II} absorptions in Fe₂(graphene–bpp) impossible.[16] A rough quantification based on the total area of the Fe $2p_{3/2}$ absorptions, yields a Fe loading of ~2.4 atm%, corresponding to ~1.7 mmol/g which is likely an overestimate.

The oxygen content of graphene–bppH and *p*-amino-bppH/graphene did not increase much compared to unfunctionalized graphene which suggests that the microwave-assisted heating is very well-tolerated and does not induce oxidative damage. In Fe₂(graphene–bpp), the [O]/[C] ratio has increased from 18.1 % to 25%, consistent with the additional presence of perchlorate and acetate ligands. The O 1s peaks at 532.1 and 533.7 eV were assigned to oxygen from carbonyl (C=O) and oxygen from ether and hydroxyl groups, respectively. The C 1s peaks at 284.8, 285.5, 288.3, 289.4, and 291.2 eV were assigned to sp² C, C-C/C=N/C-H, carbonyl (C=O), carboxyl (C(=O)-O) and aromatic *π-π** shake-up satellite carbon features, respectively.
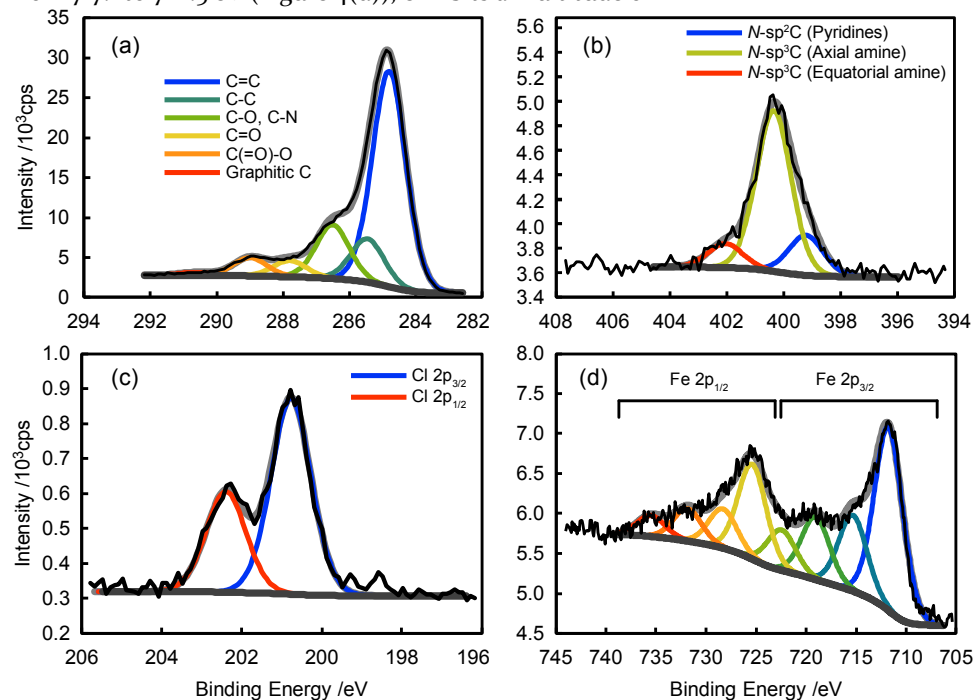

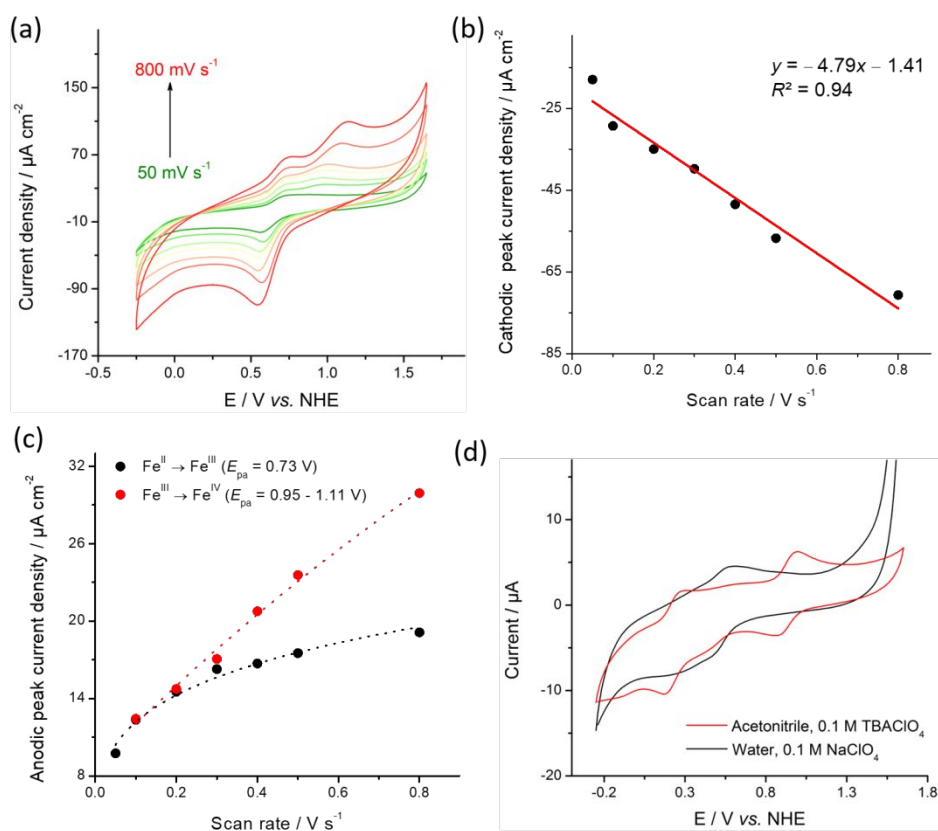Figure 4. XPS spectra of Fe₂(graphene–bpp). (**a**) C 1s, (**b**) N 1s, (**c**) Cl 2p and (**d**) Fe 2p region.

Figure 5. (**a**) Surface-confined CV of Fe$_2$(graphene–bpp)/nafion films in contact with aqueous electrolyte (0.1 M *aq*. NaClO$_4$). (**b**) Scan rate dependence of the cathodic peak current at E_p = 0.56 V with least-squares fit. (**c**) Scan rate dependencies of the anodic peak currents (dotted lines added for clarity). (**d**) CVs of the homogeneous reference compound [Fe$_2$(*tert*-butyl-bpp)(CH$_3$CO$_2$)$_2$](ClO$_4$)$_2$ (~1 mM) dissolved in water (black line) and acetonitrile (red line) with 0.1 M NaClO$_4$. Recorded at 100 mV·s^{-1}. CVs of unfunctionalized graphene/nafion on glassy carbon are shown in Supplementary Information Figure S14.

Scheme 3. Proton coupled redox processes observed for Fe$_2$(graphene–bpp)–graphene surface in aqueous solution. The curve linking the iron atoms symbolizes graphene–bpp and the structure of the resting state in box is drawn in Scheme 1.
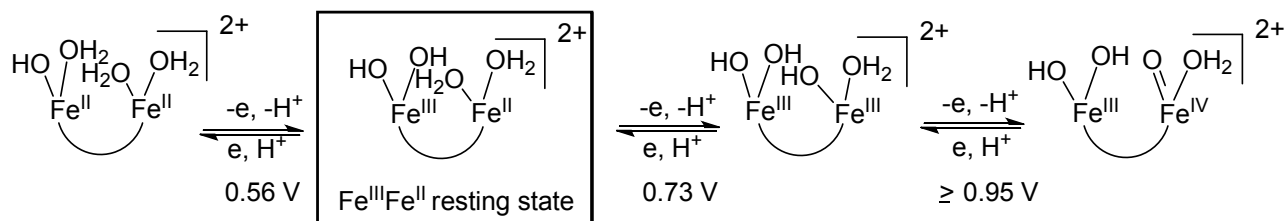
Accounting for the small amount of *N* contamination found in graphene, the [*N*]/[C] ratios for graphene–bppH and Fe$_2$(graphene–bpp) are 3.9% and 3.2%, respectively. Importantly, these ratios are 1.6-2.0 times higher than that of the physisorbed reference. Assuming that all the *N* content in the functionalized samples is due to grafted ligands, a molar loading of bpp/bppH of 0.27-0.40 mmol/g (with an average of 0.33 mmol/g) is evident for Fe$_2$(graphene–bpp) and graphene–bppH. This corresponds to the ligand and the complex making up 21.3 and 20.2 *wt*% of the functionalized samples, respectively (with an average for the two samples of 20.7 *wt*%). In comparison, a molar loading of only 0.13 mmol/g (7.0 *wt*%) was found for the physisorbed reference. These results are consistent with the bppH moieties being mainly covalently anchored to the graphene surface. We speculate that initial physisorption of the precursor material *p*-amino-bppH onto the graphene lattice might play an important role in this process.

Electrochemistry

The electrochemical behaviour of Fe$_2$(graphene–bpp) was studied by cyclic voltammetry (CV) in aqueous solution (Figure 5). The voltammograms of the resulting thin films show no particular degree of broadening and exhibit only very moderate capacitive charging components. This is true even at higher scan rates (0.8 V s$^-$

9

¹) which strongly indicates that a very thin layer has formed with a high degree of the original graphene-like nature being maintained. Line shape broadening due to porosity is otherwise a commonly observed property for modified carbon electrodes, especially when prepared by drop-casting.[61] A tilting in the orientation of the voltammograms with increased scan rate is, however, observed, which indicates the presence of some uncompensated resistance[62,63], probably arising from the double layer junction between the graphene/nafion film and the glassy carbon support. This junction resistance is likely due to the high loading of dielectric nafion ionomer needed for preparation of mechanically stable films.[64,65] The electrochemistry of Fe_2(graphene–bpp) is uniquely distinct from that of unfunctionalized graphene and graphene soaked in iron(II)-diperchlorate solutions (FeOx/graphene). The CVs of these two latter systems are available in the Supplementary Information (Figures S14 and S15). The CVs of Fe_2(graphene–bpp) reveal two irreversible oxidation waves at $E_{pa,1}$ = 0.73 V and $E_{pa,2}$ ≥ 0.95 V (*versus* the normal hydrogen electrode, NHE) together with one reduction wave at E_{pc} = 0.56 V. The reduction wave (E_{pc} = 0.56 V) and the first oxidation wave ($E_{pa,1}$ = 0.73 V) are separated by 170 mV. For a surface-confined redox process, no peak separation, or only a small one for a quasi-reversible process, is expected.[66] As such, we can conclude that these waves are not originating from the same process. This is also consistent with the asymmetric peak shape, characteristic of surface confined irreversible processes. We therefore assign the reduction wave and the first oxidation wave to, respectively, the 1 e⁻ reduction and oxidation of the $Fe^{III}Fe^{II}$ ground state (Scheme 3). The irreversibility of these waves likely derives from the aqueous medium which causes the electron transfers to occur in concert with fast proton transfers. Attempts were made to record the CVs of Fe_2(graphene–bpp) in non-protic solvents such as acetonitrile, however the nafion films were found to be unstable under these conditions.

The peak potentials for both processes are independent of the scan rate. The peak current for the $Fe^{III}Fe^{II} \rightarrow Fe^{II}Fe^{II}$ reduction wave increases linearly with the scan rate (Figure 5(b)) which is consistent with a surface confined redox process not subjected to diffusion control.[66,67] The peak current for the $Fe^{III}Fe^{II} \rightarrow Fe^{III}Fe^{III}$ oxidation wave does not show such a linear dependency on the sweep rate but levels off and becomes constant at higher scan rates (Figure 5(c)). This is probably caused by the partial overlap with the second oxidation wave (*vide infra*).

In the case of an irreversible 1 e⁻ reduction, the peak current is expected to follow Equation 3. Assuming a Laviron coefficient of α = 0.5, linear regression on a plot of the peak current for the reduction wave as a function of scan rate (Figure 5(b)) yields a surface coverage of Γ^* = 58 pmol cm⁻². This surface coverage determined from the electrochemical measurements is in good agreement with the theoretical coverage of 82 pmol cm⁻² expected from geometrical considerations available from crystal structures of these compounds.

$$I_P(v) = -\frac{\alpha \Gamma^* A F^2}{2.718 RT} v$$

Equation 3

The irreversible redox chemistry found in water for Fe_2(graphene–bpp) can be contrasted to the behaviour of the related molecular compound [Fe₂(*tert*-butyl-bpp)(CH₃CO₂)₂]²⁺ in *non*-aqueous solution where the Fe^{II}/Fe^{III} redox chemistry is reversible ($E_{1/2}$ = 0.17 V *vs.* NHE for $Fe^{III}Fe^{II}/Fe^{II}Fe^{II}$, $E_{1/2}$ = 0.88 V for $Fe^{III}Fe^{III}/Fe^{III}Fe^{II}$). Dissolution of [Fe₂(*tert*-butyl-bpp)(CH₃CO₂)₂]²⁺ in aqueous electrolyte results in the exchange of the auxiliary acetate bridging ligands for water-derived ligands, forming [Fe₂(*tert*-butyl-bpp)(OH₂)ₙ(OH)ₘ] type species. Consistently, the CVs shows a switch in the kinetics from reversible to irreversible (Figure 5(d)). The auxiliary ligand substitution introduces the possibility of associated protonation/deprotonation steps and thereby proton-coupled electron transfer kinetics, as proposed in Scheme 3. A second oxidation wave is observed in the CVs of Fe_2(graphene–bpp) at $E_{pa,2}$ ≥ 0.95 V. The peak potential and current for this process are both dependent on the scan rate (Figure 5(c)) but this process is not observed at the slowest scan rates, possibly suggesting that it is dependent on the first oxidation step. This secondary oxidation process is not resolved in the homogeneous aqueous system which suggests that the electron-rich graphene matrix could play a significant role in reducing the potential for this process and/or in stabilizing the generated high-valent species. Consistent with the high potential and the binucleating nature of the system, we assign this process to the 1 e⁻ oxidation of $Fe^{III}Fe^{III}$ to $Fe^{III}Fe^{IV}$. Again, coupled proton transfers cause irreversibility providing a reasonable explanation for the lack of observation of a corresponding reduction wave.

CONCLUSIONS

In summary, we have acheived covalent attachment of a diiron complex onto graphene and characterized the nanocomposite by a battery of bulk and surface analysis techniques. Successful functionalization was achieved through attachment of the binucleating ligand bppH by means of a microwave-facilitated diazonium coupling reaction with the diazonium salt generated *in situ* from the amino precursor ligand and isoamyl nitrite. The resulting graphene–bppH composite material was determined from XPS analysis to have an excellent average bulk loading of bppH of 0.33 mmol/g, corresponding to an average 20.7 *wt*% of the functionalized materials being made up of grafted moieties. Complexation with Fe(II)-diperchlorate in the presence of dioxygen and acetate resulted in the formation of a mixed valence $Fe^{II}Fe^{III}$ complex with the Fe(III) center existing in an S = 5/2 spin state. The covalently anchored Fe_2(bpp) moieties exhibited distinctive redox features. Notably, a $Fe^{III}Fe^{III} \rightarrow Fe^{III}Fe^{IV}$ oxidation wave was evident from the surface confined voltammograms of the grafted complex. From electrochemical measurements on Fe_2(graphene–bpp)/nafion films, a surface coverage of 58

10

pmol cm⁻² for $Fe_2(bpp)$ on graphene was observed, indicating an efficient coverage process considering the theoretically calculated coverage of 82 pmol cm⁻² derived from geometrical considerations. This electroactivity gives interesting perspectives with respect to the possibility of using the grafted system in heterogeneous electrocatalytic oxidations, *e.g.* for environmentally benign water purification.[68,69]

ASSOCIATED CONTENT

Supporting TEM/STEM images, AFM images and topological maps, supporting CVs, supporting XPS data and details on XPS grafting model, ToF-SIMS data, NMR and ESI-MS spectra of synthesized compounds are provided in the Supplementary Information. This material is available free of charge via the Internet at http://pubs.acs.org.

AUTHOR INFORMATION

Corresponding Author

* Professor T. David Waite; E-mail: d.waite@unsw.edu.au

Notes

#David de Sousa and Jeffrey Yu contributed equally to this work.

The authors declare no competing financial interests.

ORCID

T. David Waite   0000-0002-5411-3233

Christine J. McKenzie   0000-0001-5587-0626

ACKNOWLEDGMENT

REFERENCES

(1)   Geim, A. K.; Novoselov, K. S. The Rise of Graphene. *Nat Mater* **2007**, *6* (3), 183–191. https://doi.org/10.1038/nmat1849.

(2)   Brownson, D. A. C.; Kampouris, D. K.; Banks, C. E. Graphene Electrochemistry: Fundamental Concepts through to Prominent Applications. *Chem. Soc. Rev.* **2012**, *41* (21), 6944. https://doi.org/10.1039/c2cs35105f.

(3)   Marmisollé, W. A.; Azzaroni, O. Recent Developments in the Layer-by-Layer Assembly of Polyaniline and Carbon Nanomaterials for Energy Storage and Sensing Applications. From Synthetic Aspects to Structural and Functional Characterization. *Nanoscale* **2016**, *8* (19), 9890–9918. https://doi.org/10.1039/C5NR08326E.

(4)   Navalón, S.; Herance, J. R.; Álvaro, M.; García, H. Covalently Modified Graphenes in Catalysis, Electrocatalysis and Photoresponsive Materials. *Chem. - Eur. J.* **2017**, *23* (61), 15244–15275. https://doi.org/10.1002/chem.201701028.

(5)   Hu, C.; Qu, J.; Xiao, Y.; Zhao, S.; Chen, H.; Dai, L. Carbon Nanomaterials for Energy and Biorelated Catalysis: Recent Advances and Looking Forward. *ACS Cent. Sci.* **2019**, *5* (3), 389–408. https://doi.org/10.1021/acscentsci.8b00714.

(6)   Georgakilas, V.; Otyepka, M.; Bourlinos, A. B.; Chandra, V.; Kim, N.; Kemp, K. C.; Hobza, P.; Zboril, R.; Kim, K. S. Functionalization of Graphene: Covalent and Non-Covalent Approaches, Derivatives and Applications. *Chem. Rev.* **2012**, *112* (11), 6156–6214. https://doi.org/10.1021/cr3000412.

(7)   Huang, X.; Qi, X.; Boey, F.; Zhang, H. Graphene-Based Composites. *Chem Soc Rev* **2012**, *41* (2), 666–686. https://doi.org/10.1039/C1CS15078B.

(8)   Bai, H.; Li, C.; Shi, G. Functional Composite Materials Based on Chemically Converted Graphene. *Adv. Mater.* **2011**, *23* (9), 1089–1115. https://doi.org/10.1002/adma.201003753.

(9)   Avouris, P.; Chen, Z.; Perebeinos, V. Carbon-Based Electronics. *Nat. Nanotechnol.* **2007**, *2* (10), 605–615.

(10)   Salavagione, H. J.; Martínez, G.; Ellis, G. Recent Advances in the Covalent Modification of Graphene With Polymers. *Macromol. Rapid Commun.* **2011**, *32* (22), 1771–1789. https://doi.org/10.1002/marc.201100527.

(11)   Dyke, C. A.; Tour, J. M. Solvent-Free Functionalization of Carbon Nanotubes. *J. Am. Chem. Soc.* **2003**, *125* (5), 1156–1157. https://doi.org/10.1021/ja0289806.

(12)   Liu, J.; Zubiri, M. R.; Vigolo, B.; Dossot, M.; Humbert, B.; Fort, Y.; McRay, E. Microwave-Assisted Functionalization of Single-Wall Carbon Nanotubes Through Diazonium. *J. Nanosci. Nanotechnol.* **2007**, *7*, 3519–3523. https://doi.org/10.1166/jnn.2007.819.

(13)   Brunetti, F. G.; Herrero, M. A.; Muñoz, J. de M.; Díaz-Ortiz, A.; Alfonsi, J.; Meneghetti, M.; Prato, M.; Vázquez, E. Microwave-Induced Multiple Functionalization of Carbon Nanotubes. *J. Am. Chem. Soc.* **2008**, *130* (25), 8094–8100. https://doi.org/10.1021/ja801971k.

(14)   Castelaín, M.; Shuttleworth, P. S.; Marco, C.; Ellis, G.; Salavagione, H. J. Comparative Study of the Covalent Diazotization of Graphene and Carbon Nanotubes Using Thermogravimetric and Spectroscopic Techniques. *Phys. Chem. Chem. Phys.* **2013**, *15* (39), 16806–16811. https://doi.org/10.1039/c3cp52672k.

(15)   Ragoussi, M.-E.; Malig, J.; Katsukis, G.; Butz, B.; Spiecker, E.; de la Torre, G.; Torres, T.; Guldi, D. M. Linking Photo- and Redoxactive Phthalocyanines Covalently to Graphene. *Angew. Chem. Int. Ed.* **2012**, *51* (26), 6421–6425. https://doi.org/10.1002/anie.201201452.

(16)   Fortgang, P.; Tite, T.; Barnier, V.; Zehani, N.; Maddi, C.; Lagarde, F.; Loir, A.-S.; Jaffrezic-Renault, N.; Donnet, C.; Garrelie, F.; et al. Robust Electrografting on Self-Organized 3D Graphene Electrodes. *ACS Appl. Mater. Interfaces* **2016**, *8* (2), 1424–1433. https://doi.org/10.1021/acsami.5b10647.

(17)   Xu, Y.; Liu, Z.; Zhang, X.; Wang, Y.; Tian, J.; Huang, Y.; Ma, Y.; Zhang, X.; Chen, Y. A Graphene Hybrid Material Covalently Functionalized with Porphyrin: Synthesis and Optical Limiting Property. *Adv. Mater.* **2009**, *21* (12), 1275–1279. https://doi.org/10.1002/adma.200801617.

(18)   Dey, R. S.; Raj, C. R. Redox-Functionalized Graphene Oxide Architecture for the Development of Amperometric Biosensing Platform. *ACS Appl. Mater. Interfaces* **2013**, *5* (11), 4791–4798. https://doi.org/10.1021/am400280u.

(19)   Stergiou, A.; Pagona, G.; Tagmatarchis, N. Donor–Acceptor Graphene-Based Hybrid Materials Facilitating Photo-Induced Electron-Transfer Reactions. *Beilstein J. Nanotechnol.* **2014**, *5*, 1580–1589. https://doi.org/10.3762/bjnano.5.170.

11

(20)   Wibmer, L.; Lourenco, L. M. O.; Roth, A.; Katsukis, G.; Neves, M. G. P. M. S.; Cavaleiro, J. A. S.; Tome, J. P. C.; Torres, T.; Guldi, D. M. Decorating Graphene Nanosheets with Electron Accepting Pyridyl-Phthalocyanines. *Nanoscale* **2015**, *7* (13), 5674–5682. https://doi.org/10.1039/C4NR05719H.

(21)   Sun, C.; Li, Z.; Zhong, X.; Wang, S.; Yin, X.; Wang, L. Three-Dimensional Graphene-Supported Cobalt Phthalocyanine as Advanced Electrocatalysts for Oxygen Reduction Reaction. *J. Electrochem. Soc.* **2018**, *165* (2), F24–F31. https://doi.org/10.1149/2.0521802jes.

(22)   Zhao, Q.; Li, Y.; Liu, R.; Chen, A.; Zhang, G.; Zhang, F.; Fan, X. Enhanced Hydrogenation of Olefins and Ketones with a Ruthenium Complex Covalently Anchored on Graphene Oxide. *J. Mater. Chem. A* **2013**, *1* (47), 15039–15045. https://doi.org/10.1039/C3TA13378H.

(23)   Li, X.; Hao, Z.; Zhang, F.; Li, H. Reduced Graphene Oxide-Immobilized Tris(Bipyridine)Ruthenium(II) Complex for Efficient Visible-Light-Driven Reductive Dehalogenation Reaction. *ACS Appl. Mater. Interfaces* **2016**, *8* (19), 12141–12148. https://doi.org/10.1021/acsami.6b01100.

(24)   Meng, T. T.; Xue, L. X.; Wang, H.; Wang, K. Z.; Haga, M. PH Controllable Photocurrent Switching and Molecular Half-Subtractor Calculations Based on a Monolayer Composite Film of a Dinuclear Ru II Complex and Graphene Oxide. *J. Mater. Chem. C* **2017**, 5 (13), 3390–3396. https://doi.org/10.1039/C7TC00494J.

(25)   Song Shungang; Xue Yuhua; Feng Lianfang; Elbatal Hany; Wang Pingshan; Moorefield Charles N.; Newkome George R.; Dai Liming. Reversible Self-Assembly of Terpyridine-Functionalized Graphene Oxide for Energy Conversion. *Angew. Chem. Int. Ed.* **2013**, 53 (5), 1415–1419. https://doi.org/10.1002/anie.201309641.

(26)   Ghasemi, E.; Alimardani, E.; Shams, E.; Koohmareh, G. A. Modification of Glassy Carbon Electrode with Iron-Terpyridine Complex and Iron-Terpyridine Complex Covalently Bonded to Ordered Mesoporous Carbon Substrate: Preparation, Electrochemistry and Application to H $_2$ O $_2$ Determination. *J. Electroanal. Chem.* **2017**, *789*, 92–99. https://doi.org/10.1016/j.jelechem.2017.01.043.

(27)   Kalita, G.; Sharma, S.; Wakita, K.; Umeno, M.; Hayashi, Y.; Tanemura, M. A Photoinduced Charge Transfer Composite of Graphene Oxide and Ferrocene. *Phys. Chem. Chem. Phys.* **2013**, *15* (4), 1271–1274. https://doi.org/10.1039/C2CP43427J.

(28)   Mosconi, D.; Blanco, M.; Gatti, T.; Calvillo, L.; Otyepka, M.; Bakandritsos, A.; Menna, E.; Agnoli, S.; Granozzi, G. Arene C H Insertion Catalyzed by Ferrocene Covalently Heterogenized on Graphene Acid. *Carbon* **2019**, *143*, 318–328. https://doi.org/10.1016/j.carbon.2018.11.010.

(29)   Wang, Q.; Lei, J.; Deng, S.; Zhang, L.; Ju, H. Graphene-Supported Ferric Porphyrin as a Peroxidase Mimic for Electrochemical DNA Biosensing. *Chem. Commun.* **2013**, *49* (9), 916–918. https://doi.org/10.1039/C2CC37664D.

(30)   Choucair, M.; Thordarson, P.; Stride, J. A. Gram-Scale Production of Graphene Based on Solvothermal Synthesis and Sonication. *Nat. Nanotechnol.* **2008**, *4*, 30–33.

(31)   Park, S.; Ruoff, R. S. Chemical Methods for the Production of Graphenes. *Nat. Nanotechnol.* **2009**, *4*, 217–224.

(32)   Lei, Z.; Zhang, J.; Zhang, L. L.; Kumar, N. A.; Zhao, X. S. Functionalization of Chemically Derived Graphene for Improving Its Electrocapacitive Energy Storage Properties. *Energy Environ. Sci.* **2016**, *9* (6), 1891–1930. https://doi.org/10.1039/C6EE00158K.

(33)   Vázquez, E.; Prato, M. Carbon Nanotubes and Microwaves: Interactions, Responses, and Applications. *ACS Nano* **2009**, 3 (12), 3819–3824. https://doi.org/10.1021/nn901604j.

(34)   Kong, N.; Park, J.; Yang, X.; Ramström, O.; Yan, M. Carbohydrate Functionalization of Few-Layer Graphene through

Microwave-Assisted Reaction of Perfluorophenyl Azide. *ACS Appl. Bio Mater.* **2019**, *2* (1), 284–291. https://doi.org/10.1021/acsabm.8b00597.

(35)   Bahr, J. L.; Tour, J. M. Highly Functionalized Carbon Nanotubes Using in Situ Generated Diazonium Compounds. *Chem. Mater.* **2001**, *13* (11), 3823–3824. https://doi.org/10.1021/cm0109903.

(36)   Ghiladi, M.; McKenzie, C. J.; Meier, A.; Powell, A. K.; Ulstrup, J.; Wocadlo, S. Dinuclear Iron(III)–Metal(II) Complexes as Structural Core Models for Purple Acid Phosphatases. *J. Chem. Soc. Dalton Trans.* **1997**, *25* (21), 4011–4018. https://doi.org/10.1039/A704388K.

(37)   Ghiladi, M.; Jensen, K. B.; Jiang, J.; McKenzie, C. J.; Mørup, S.; Søtofte, I.; Ulstrup, J. Synthesis and Characterization of Dinuclear Complexes Containing the FeIII–F· · ·(H2O)MII Motif. *J. Chem. Soc. Dalton Trans.* **1999**, *27* (16), 2675–2681. https://doi.org/10.1039/A902678I.

(38)   Xu, B.; Zhong, W.; Wei, Z.; Wang, H.; Liu, J.; Wu, L.; Feng, Y.; Liu, X. Iron(III) Complexes of Multidentate Pyridinyl Ligands: Synthesis, Characterization and Catalysis of the Direct Hydroxylation of Benzene. *Dalton Trans.* **2014**, *43* (41), 15337–15345. https://doi.org/10.1039/C4DT02032D.

(39)   Singh, R.; Haukka, M.; McKenzie, C. J.; Nordlander, E. High Turnover Catalase Activity of a Mixed-Valence Mn(II)Mn(III) Complex with Terminal Carboxylate Donors: High Turnover Catalase Activity of a Mixed-Valence Mn(II)Mn(II) Complex. *Eur. J. Inorg. Chem.* **2015**, *2015* (21), 3485–3492. https://doi.org/10.1002/ejic.201500468.

(40)   Hanania, G. I.; Irvine, D. H.; Eaton, W. A.; George, P. Thermodynamic Aspects of the Potassium Hexacyano-Ferrate (III)-(II) System. II. Reduction Potential. *J. Phys. Chem.* **1967**, *71* (7), 2022–2030.

(41)   McCreery, R. L. Advanced Carbon Electrode Materials for Molecular Electrochemistry. *Chem. Rev.* **2008**, *108* (7), 2646–2687. https://doi.org/10.1021/cr068076m.

(42)   Lee, L.; Leroux, Y. R.; Hapiot, P.; Downard, A. J. Amine-Terminated Monolayers on Carbon: Preparation, Characterization, and Coupling Reactions. *Langmuir* **2015**, *31* (18), 5071–5077. https://doi.org/10.1021/acs.langmuir.5b00730.

(43)   Yang, S.; Feng, G.; Williams, N. H. Highly Selective Colorimetric Sensing Pyrophosphate in Water by a NBD-Phenoxo-Bridged Dinuclear Zn(II) Complex. *Org. Biomol. Chem.* **2012**, *10* (29), 5606–5612. https://doi.org/10.1039/C2OB25617G.

(44)   Nemes-Incze, P.; Osváth, Z.; Kamarás, K.; Biró, L. P. Anomalies in Thickness Measurements of Graphene and Few Layer Graphite Crystals by Tapping Mode Atomic Force Microscopy. *Carbon* **2008**, *46* (11), 1435–1442. https://doi.org/10.1016/j.carbon.2008.06.022.

(45)   Li, D.; Zhou, J.; Chen, X.; Song, H. Amorphous Fe2O3/Graphene Composite Nanosheets with Enhanced Electrochemical Performance for Sodium-Ion Battery. *ACS Appl. Mater. Interfaces* **2016**, *8* (45), 30899–30907. https://doi.org/10.1021/acsami.6b09444.

(46)   Wang, Z.; Liu, C.-J. Preparation and Application of Iron Oxide/Graphene Based Composites for Electrochemical Energy Storage and Energy Conversion Devices: Current Status and Perspective. *Nano Energy* **2015**, *11*, 277–293. https://doi.org/10.1016/j.nanoen.2014.10.022.

(47)   Li, Y.; Huang, J.; Hu, X.; Bi, L.; Cai, P.; Jia, J.; Chai, G.; Wei, S.; Dai, L.; Wen, Z. Fe Vacancies Induced Surface FeO $_6$ in Nanoarchitectures of N-Doped Graphene Protected β-FeOOH: Effective Active Sites for PH-Universal Electrocatalytic Oxygen Reduction. *Adv. Funct. Mater.* **2018**, *28* (34), 1803330. https://doi.org/10.1002/adfm.201803330.

(48)   Xiang, Z.; Dai, Q.; Chen, J.-F.; Dai, L. Edge Functionalization of Graphene and Two-Dimensional Covalent Organic Polymers for Energy Conversion and Storage. *Adv. Mater.* **2016**, *28* (29), 6253–6261. https://doi.org/10.1002/adma.201505788.

(49)   Tampieri, F.; Silvestrini, S.; Riccò, R.; Maggini, M.; Barbon, A. A Comparative Electron Paramagnetic Resonance Study of Expanded Graphites and Graphene. *J Mater Chem C* **2014**, *2* (38), 8105–8112. https://doi.org/10.1039/C4TC01383B.

(50)   Diamantopoulou, A.; Glenis, S.; Zolnierkiwicz, G.; Guskos, N.; Likodimos, V. Magnetism in Pristine and Chemically Reduced Graphene Oxide. *J. Appl. Phys.* **2017**, *121* (4), 043906. https://doi.org/10.1063/1.4974364.

(51)   Kausteklis, J.; Cevc, P.; Arčon, D.; Nasi, L.; Pontiroli, D.; Mazzani, M.; Riccò, M. Electron Paramagnetic Resonance Study of Nanostructured Graphite. *Phys. Rev. B* **2011**, *84* (12), 125406. https://doi.org/10.1103/PhysRevB.84.125406.

(52)   Ćirić, L.; Sienkiewicz, A.; Djokić, D. M.; Smajda, R.; Magrez, A.; Kaspar, T.; Nesper, R.; Forró, L. Size Dependence of the Magnetic Response of Graphite Oxide and Graphene Flakes - an Electron Spin Resonance Study. *Phys. Status Solidi B* **2010**, *247* (11–12), 2958–2961. https://doi.org/10.1002/pssb.201000448.

(53)   Brant, P.; Feltham, R. D. An X-Ray Photoelectron Spectral Study of Iron and Cobalt Nitrosyl Complexes of o-Phenylenebis (Dimethylarsine). *Inorg. Chem.* **1980**, *19* (9), 2673–2676.

(54)   Gammon, W. J.; Kraft, O.; Reilly, A. C.; Holloway, B. C. Experimental Comparison of N (1s) X-Ray Photoelectron Spectroscopy Binding Energies of Hard and Elastic Amorphous Carbon Nitride Films with Reference Organic Compounds. *Carbon* **2003**, *41* (10), 1917–1923.

(55)   Artyushkova, K.; Kiefer, B.; Halevi, B.; Knop-Gericke, A.; Schlogl, R.; Atanassov, P. Density Functional Theory Calculations of XPS Binding Energy Shift for Nitrogen-Containing Graphene-like Structures. *Chem. Commun.* **2013**, *49* (25), 2539–2541. https://doi.org/10.1039/c3cc40324f.

(56)   Axet, M. R.; Dechy-Cabaret, O.; Durand, J.; Gouygou, M.; Serp, P. Coordination Chemistry on Carbon Surfaces. *Coord. Chem. Rev.* **2016**, *308*, 236–345. https://doi.org/10.1016/j.ccr.2015.06.005.

(57)   Georgakilas, V.; Tiwari, J. N.; Kemp, K. C.; Perman, J. A.; Bourlinos, A. B.; Kim, K. S.; Zboril, R. Noncovalent Functionalization of Graphene and Graphene Oxide for Energy Materials, Biosensing, Catalytic, and Biomedical Applications. *Chem. Rev.* **2016**, *116* (9), 5464–5519. https://doi.org/10.1021/acs.chemrev.5b00620.

(58)   Zuo, X.; Chang, K.; Zhao, J.; Xie, Z.; Tang, H.; Li, B.; Chang, Z. Bubble-Template-Assisted Synthesis of Hollow Fullerene-like MoS$_2$ Nanocages as a Lithium Ion Battery Anode Material. *J. Mater. Chem. A* **2016**, *4* (1), 51–58. https://doi.org/10.1039/C5TA06869J.

(59)   Grosvenor, A. P.; Kobe, B. A.; Biesinger, M. C.; McIntyre, N. S. Investigation of Multiplet Splitting of Fe 2p XPS Spectra and Bonding in Iron Compounds. *Surf. Interface Anal.* **2004**, *36* (12), 1564–1574. https://doi.org/10.1002/sia.1984.

(60)   Kozakov, A. T.; Kochur, A. G.; Googlev, K. A.; Nikolsky, A. V.; Raevski, I. P.; Smotrakov, V. G.; Yeremkin, V. V. X-Ray Photoelectron Study of the Valence State of Iron in Iron-Containing Single-Crystal (BiFeO3, PbFe1/2Nb1/2O3), and Ceramic (BaFe1/2Nb1/2O3) Multiferroics. *J. Electron Spectrosc. Relat. Phenom.* **2011**, *184* (1), 16–23. https://doi.org/10.1016/j.elspec.2010.10.004.

(61)   Punckt, C.; Pope, M. A.; Aksay, I. A. On the Electrochemical Response of Porous Functionalized Graphene Electrodes. *J. Phys. Chem. C* **2013**, *117* (31), 16076–16086. https://doi.org/10.1021/jp405142k.

(62)   Unjaroen, D.; Swart, M.; Browne, W. R. Electrochemical Polymerization of Iron(III) Polypyridyl Complexes through C–C Coupling of Redox Non-Innocent Phenolato Ligands. *Inorg. Chem.* **2017**, *56* (1), 470–479. https://doi.org/10.1021/acs.inorgchem.6b02378.

(63)   Henstridge, M. C.; Batchelor-McAuley, C.; Gusmão, R.; Compton, R. G. Marcus–Hush–Chidsey Theory of Electron Transfer to and from Species Bound at a Non-Uniform Electrode Surface: Theory and Experiment. *Chem. Phys. Lett.* **2011**, *517* (1–3), 108–112. https://doi.org/10.1016/j.cplett.2011.10.023.

(64)   Kim, Y.; Ketpang, K.; Jaritphun, S.; Park, J. S.; Shanmugam, S. A Polyoxometalate Coupled Graphene Oxide–Nafion Composite Membrane for Fuel Cells Operating at Low Relative Humidity. *J Mater Chem A* **2015**, *3* (15), 8148–8155. https://doi.org/10.1039/C5TA00182J.

(65)   Xi, J.; Wu, Z.; Teng, X.; Zhao, Y.; Chen, L.; Qiu, X. Self-Assembled Polyelectrolyte Multilayer Modified Nafion Membrane with Suppressed Vanadium Ion Crossover for Vanadium Redox Flow Batteries. *J. Mater. Chem.* **2008**, *18* (11), 1232–1238. https://doi.org/10.1039/B718526J.

(66)   Bard, A. J.; Faulkner, L. R. *Electrochemical Methods and Applications*; Wiley-Interscience: New York; London, 2000.

(67)   Wang, J.; Sun, H.; Zhao, X. S. Electrochemical Catalysis and Stability of Tetraamido Macrocyclic Ligands Iron Immobilized on Modified Pyrolytic Graphite Electrode. *Catal. Today* **2010**, *158* (3–4), 263–268. https://doi.org/10.1016/j.cattod.2010.03.046.

(68)   de Sousa, D. P.; Miller, C. J.; Chang, Y.; Waite, T. D.; McKenzie, C. J. Electrochemically Generated Cis-Carboxylato-Coordinated Iron(IV) Oxo Acid–Base Congeners as Promiscuous Oxidants of Water Pollutants. *Inorg. Chem.* **2017**, 14936–14947. https://doi.org/10.1021/acs.inorgchem.7b02208.

(69)   Miller, C. J.; Wadley, S.; Waite, T. D. Fenton, Photo-Fenton and Fenton-like Processes. In *Advanced Oxidation Processes for Water Treatment: Fundamentals and Applications*; IWA Publishing, 2017.

13

Table of Contents Graphical Abstract